Title

Reversible Room-Temperature Fluoride-Ion Insertion in a Tunnel-Structured Transition Metal Oxide Host

Journal

ACS Energy Letters, 5(8)

ISSN

2380-8195

Authors

Zaheer, Wasif
Andrews, Justin L
Parija, Abhishek
et al.

Publication Date

2020-08-14

DOI

10.1021/acsenergylett.0c01328

Reversible Room-Temperature Fluoride-Ion Insertion in a Tunnel-Structured Transition Metal Oxide Host

Wasif Zaheer,[†,‡] Justin L. Andrews,[†] Abhishek Parija,[†,‡] Forrest P. Hyler,[§] Jaye Cherno,[⊥] Conan Weiland,[⊥] David A. Shapiro,[‡] Jinghua Guo,[‡] Jesús M. Velázquez,[§] and Sarbajit Banerjee[†]*

† Department of Chemistry and Department of Material Science and Engineering, Texas A&M University, College Station, TX 77845-3012 (USA); *banerjee@chem.tamu.edu

‡ Advanced Light Source, Lawrence Berkeley National Laboratory, 1 Cyclotron Road, Berkeley California 94720, United States

§ Department of Chemistry, University of California, Davis, Davis, CA, USA

⊥National Synchrotron Light Source II, Brookhaven National Lab, 98 Rochester St, Upton, NY 11973, United States

ABSTRACT

An energy storage paradigm orthogonal to conventional Li-ion battery chemistries can be conceptualized by employing anions as the primary charge carriers. Fluoride-ion conversion battery chemistries show promise but have limited cyclability as a result of the significant change in volume of active electrodes upon metal–metal-fluoride interconversion. In contrast, the exploration of insertion chemistries has been stymied by the lack of insertion hosts that can reversibly insert fluoride-ions at room temperature. Here we show the reversible and homogeneous topochemical insertion and extraction of F-ions within the 1D tunnels of submicron-sized $FeSb_2O_4$ particles at room temperature. The insertion of F-ions brings about a formal oxidation of iron centers from a divalent to a trivalent formal oxidation state and brings about a <1% contraction of the lattice volume at a capacity of one fluoride-ion per iron center. The topochemical insertion of fluoride-ions is observed to be homogenous across the $FeSb_2O_4$ particles. The design principles noted here suggest an approach to designing oxidative insertion hosts that fulfill the distinctive needs of anion batteries.

INTRODUCTION

Li-ion batteries have emerged as the dominant energy storage paradigm for electromobility and consumer electronics applications. [1,2] However, with demands for energy storage trending sharply upwards across a diverse range of applications, there is increasing emphasis not just on conventional performance metrics such as energy and power density but on technological diversity, materials criticality, and the identification of energy storage concepts that satisfy the resource constraints and power needs of specific intended applications.[3] As such, substantial efforts have focused on

the exploration of alternative “beyond lithium-ion” monovalent (e.g., Na^+, K^+) and multivalent (e.g., Mg^{2+}, Ca^{2+}, and Al^{3+}) insertion and conversion battery chemistries.[4–7] An intriguing orthogonal energy storage paradigm can be conceptualized by employing anions as the primary charge carriers. In particular, fluoride-ion conversion chemistries have received recent attention.[8,9] Fluoride-ion conversion batteries are predicated on the shuttling of F-ions between metal/metal-fluoride electrodes but show relatively poor cycle life as a result of the large volume changes accompanying metal-metal fluoride conversion reactions.[10] In contrast, the insertion chemistry of F-ions remains poorly developed. In analogy with Li-ion batteries, F-ion insertion requires insertion hosts with a large abundance of interstitial sites, accessible redox centers, and the ability to accommodate the inserted ions without large lattice dilation; however, an important difference is that F-ion insertion reactions must bring about oxidation and not reduction of the redox sites. Here, we demonstrate the reversible solution-phase insertion/extraction of F-ions from a tunnel-structured p—d-block insertion host, $FeSb_2O_4$, evidencing the reversible oxidation/reduction of iron centers upon F-ion insertion/de-insertion.

F-ion insertion within redox-active frameworks has thus far required high temperatures and gas-phase reactions.[11,12] Despite the evident promise of fluoride-ion batteries to serve as low-cost energy storage vectors, scarce little is known about mechanisms of F-ion insertion. The repertoire of electrode materials that can reversibly insert F-ions furthermore remains exceedingly sparse and role of finite size effects in improving ion diffusion remains to be explored.[13] In this work, we demonstrate reversible room-temperature topochemical insertion of F-ions in hydrothermally synthesized $FeSb_2O_4$ rods.[14] The particles with a rod-like morphology have been prepared as described in the Supporting Information by the reaction of $FeSO_4(NH_4)_2SO_4.6H_2O$ and $SbCl_3$ in basic solution as per:

Figure 1 shows the structure of $FeSb_2O_4$ refined from the powder X-ray diffraction pattern shown in **Figure 2A**. The XRD further attests to the phase purity of the hydrothermally prepared materials. $FeSb_2O_4$ crystallizes in a tetragonal space group ($P4_2mbc$, $\boldsymbol{a} = \boldsymbol{b} =$ 8.5807Å, $\boldsymbol{c} =$ 5.9131Å). The $FeSb_2O_4$ structure consists of edge-sharing FeO_6 octahedra connected to SbO_3 tetrahedra with one vertex occupied by its lone pair of electrons. The resulting coordinative unsaturation of Sb opens up a rigid one-dimensional channel along the [001] direction. The lattice constants, atom positions, and refinement statistics are provided in **Table S1**. **Figure S1** shows SEM and

TEM images of the $FeSb_2O_4$ particles, which are crystallized in a faceted rod-like morphology with diameters ranging from 200 to 350 nm and spanning *ca.* 1 to 2 µm in length with some platelets discernible at the edges of the facets.

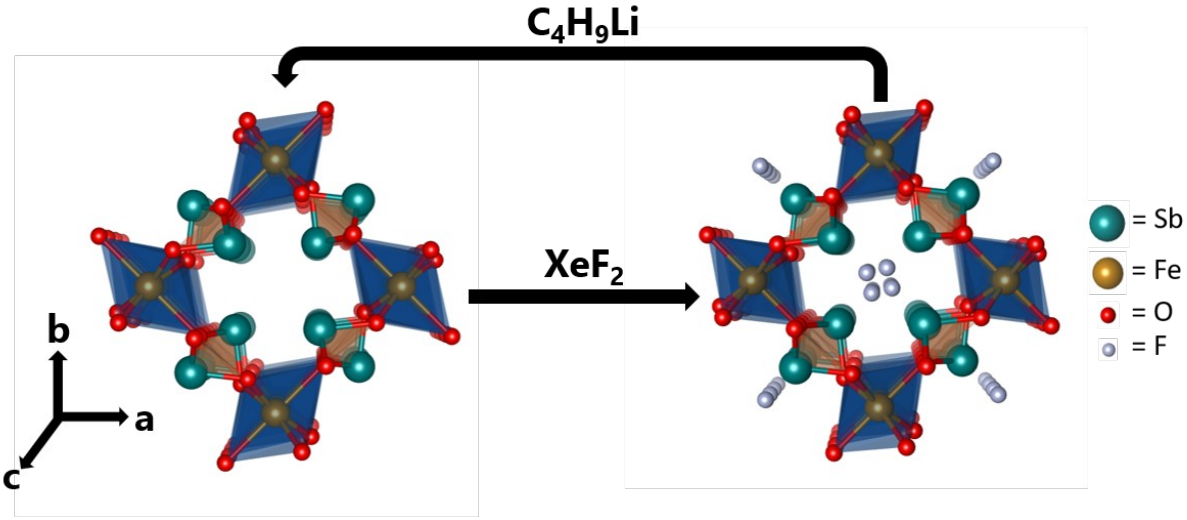

Figure 1. Illustration of the reversible topochemical intercalation of fluoride-ions in $FeSb_2O_4$ depicting the refined crystal structures of the starting and topochemically F-ion inserted phases.

Topotactic F-ion insertion has been performed by stirring the hydrothermally synthesized $FeSb_2O_4$ rods with a molar excess of XeF_2 in acetonitrile at 23°C as per:

XeF_2 is a powerful fluoridating agent, which by dint of its high solubility in organic solvents enables a high local chemical activity of fluoride-ion precursors to be established at the solid/liquid interface.[15] In comparison to analogous inorganic salts where the cation can act as a secondary intercalant,[14] XeF_2 provides a clean source of F-ions, enabling unambiguous characterization of the inserted products.

Figure 2B shows a refinement of powder XRD data collected for the sample fluoridated at room temperature, corresponding to a nominal stoichiometry of $x = 1 \pm 0.05$ in $FeSb_2O_4F_x$, albeit considerable disorder is observed in F-ion sites (**Table S2**). Comparison of powder XRD patterns of the fluoridated samples with the starting $FeSb_2O_4$ reveals preservation of the tetragonal symmetry but with some notable changes. The reflections from the {002} planes appear at lower 2θ values as compared to the reflections

from {220} and the reflections from the {112} planes are shifted to lower 2θ values as compared to the reflections from {310} planes, suggesting an anisotropic expansion of the tunnel such that the SbO_3 polyhedra are buckled inwards and the FeO_6 octahedra are pressed outwards (*vide infra*). An 80°C treatment allows the F-ions to find their lowest energy interstitial sites. **Figure S2** shows powder XRD data and its refinement that allows for identification of the F-ion crystallographic sites within the tunnel as shown in **Figure 1** (**Tables S3** and **S4**). The tunnels serve as channels for diffusion of F-ions along interstitial sites bounded by Sb atoms. Overall, F-ion insertion induces a slight contraction of the lattice (<1%); the observed lattice contraction manifests the consequences of oxidative insertion and represents a lattice dilation typically observed in the case of Li-ion insertion. The ***a*** and ***b*** lattice parameters shrink upon F-ion insertion, whereas the ***c*** parameter is increased. The position of F-ions is slightly off-centered from the tetrahedral site created by four Sb atoms as depicted in **Figure 1**. This off-centering is indicative of stabilization of F-ions as a result of preferred coordination to one of the four Sb atoms. Changes in the average structure of $FeSb_2O_4$ as a result of fluoridation are visualized in **Videos S1** and **S2**.

Modifications of the local atomistic structure as a result of fluoridation have been further evidenced using extended X-ray absorption fine structure (EXAFS) spectroscopy at the Fe K-edge. Shell fitting for EXAFS data has been performed starting from the atomic coordinates obtained from Rietveld refinements of the powder XRD data. Fourier-transformed R-space EXAFS data for $FeSb_2O_4$, $FeSb_2O_4F_x$ (x ~1) and their difference is plotted in **Figure 2D**. Three prominent features are assigned as follows: the correlation at ~2.1Å is fitted to Fe-$O_{eq.}$ (equatorial) and Fe-$O_{ax.}$ (axial) paths; the correlation at ~3.0Å is attributed to the Fe—Fe separation; and the ~3.5Å feature is assigned to a Fe—Sb path. Upon fluoridation, the Fe-O bonds are significantly decreased in length. The Fe-$O_{ax.}$ bond lengths decrease from 2.350Å to 2.094Å, whereas the Fe-$O_{eq.}$ bond distances decrease from 2.072Å to 1.968Å, reflective of oxidation of divalent iron to trivalent iron **Figure 2F** shows models of FeO_6 octahedra constructed using the Fe-O distances derived from fitting the EXAFS data in **Figures S3**-**S5** (**Tables S5** and **S6**). The local structure data is in excellent agreement with the average structured gleaned from analysis of the powder XRD data but further delineates the local distortions of the FeO_6 coordination environment as a result of oxidative F-ion insertion.

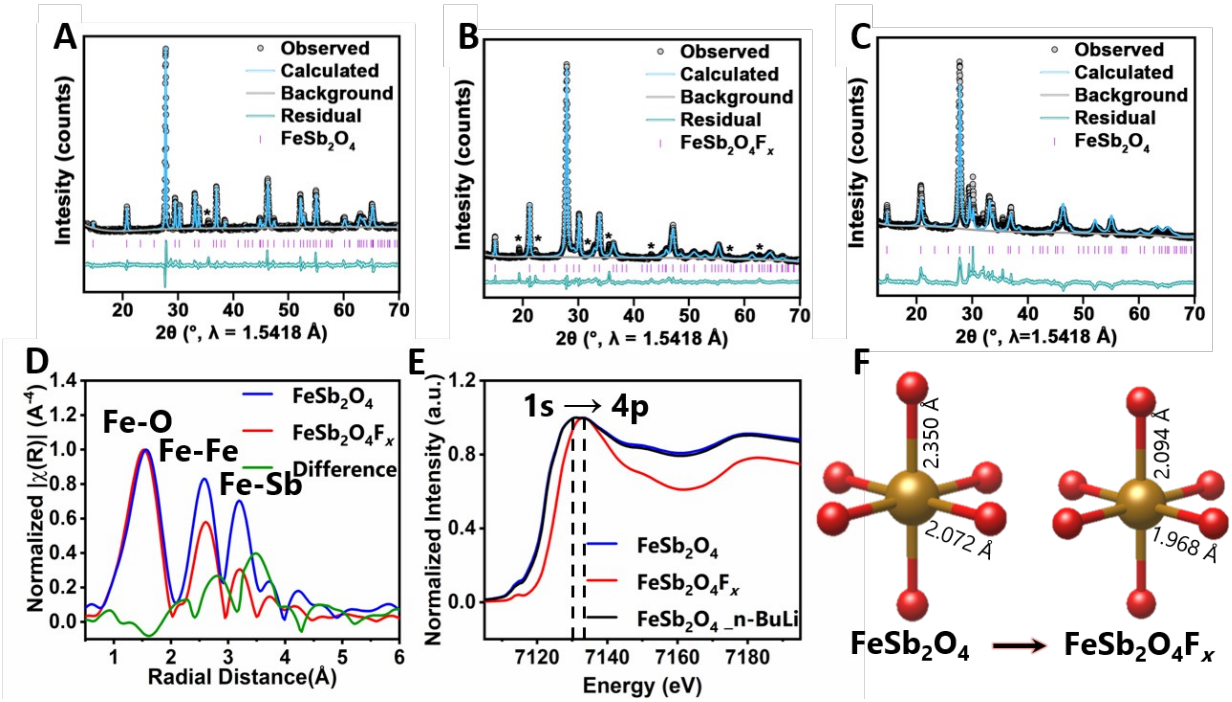

Figure 2. *Structural Characterization of $FeSb_2O_4$ upon Fluoridation.* A-C) Powder XRD patterns and Rietveld refinement profiles for $FeSb_2O_4$, $FeSb_2O_4F_x$ (x~1), prepared by room-temperature fluoridation), and $FeSb_2O_4$ recovered after treatment with *n*-BuLi. The collected diffraction data is shown as black-outlined grey circles, the Rietveld fit is shown as a solid light blue line, the Chebyshev polynomial background fit is shown as a solid light grey line, the residual (observed - Rietveld fit) is shown as a solid teal line, and the calculated positions of reflections for the two $FeSb_2O_4F_x$ phases are shown in magenta. D) k^3-weighted Fourier-transformed R-space data extracted from Fe K-edge EXAFS spectra for $FeSb_2O_4$ and $FeSb_2O_4F_x$ (x~1) alongside their difference spectrum. E) Comparison of Fe K-edge XANES spectra for $FeSb_2O_4$ and $FeSb_2O_4F_x$ (F) FeO_6 models generated from fitted EXAFS data for $FeSb_2O_4$ and $FeSb_2O_4F_x$ (Key: Fe = gold O = red).

To evidence the reversibility of the F-ion insertion, the $FeSb_2O_4F_x$ sample was stirred in a solution of *n*-BuLi in hexanes at 23°C to recover the $FeSb_2O_4$ as per:

$$FeSb_2O_4F_x(s) + x\,C_4H_9Li(hexanes) \xrightarrow[24\,h]{23\,^{\circ}C} FeSb_2O_4(s) + x\,LiF(s) + \tfrac{x}{2}\,C_8H_{18}(l)\,(g) \quad (3)$$

The LiF byproduct was removed by washing with hexanes. The removal of the inserted F-ions restores the lattice to its original state. A powder XRD pattern obtained for the deintercalated sample is presented in **Figure 2C**.

Refinement of the powder XRD pattern shows a recovery of the undistorted $FeSb_2O_4$ crystal lattice. The refined lattice parameters (***a* = *b* =** 8.5684(9)Å**, *c* =** 5.9315(12) Å) suggest the near-complete removal of F-ions from the lattice (**Table S7)**. Indeed, the Fe K-edge XANES spectra of the pristine and F-ion extracted sample in Figure **3E** are exactly superimposable. The Fe-O bond distances deduced from the fitting of EXAFS data are further recovered upon defluoridation with *n*-BuLi with Fe-$O_{eq.}$ and Fe-$O_{ax.}$ distances of 2.060Å and 2.340Å, respectively. The facile deintercalation of the F-ions at room temperature attests to the reversibility expunging of F-ions in solution phase for submicron-sized $FeSb_2O_4$ particles.

X-ray absorption and emission spectroscopies have been used to probe the electronic structure implications of F-ion insertion and extraction. Analysis of the Fe K-edge XANES spectra in **Figure 2E** shows that the primary absorption feature attributed to a Fe 1s→Fe 4p transition is shifted from *ca.* 7130 eV in $FeSb_2O_4$ to *ca.* 7133 eV in $FeSb_2O_4F_x$ (x ~1) indicative of the oxidation of divalent iron to trivalent iron.[16] F K-edge XANES measurements in **Figure S6A** further confirm the insertion of ionic fluoride species.[17] Based on the relative ratios of Fe L_{III} and Fe L_{II} features in the Fe L-edge XANES spectrum in **Figure S6A**, a trivalent oxidation state can be inferred for the iron centers after F-ion insertion.[18] The increased oxidation state of Fe underpins the shrinkage of Fe-O bonds observed in the EXAFS measurements and is further consistent with an increased Fe—Fe distance manifested as an observed increase in the ***c*** parameter measured by powder X-ray diffraction.

Contiguous Sb M-edge and O K-edge XANES spectra for $FeSb_2O_4$ and $FeSb_2O_4F_x$ (x ~1) are plotted in **Figure S6B**. Since Sb atoms have a trigonal-pyramidal geometry in $FeSb_2O_4$, a strong pre-edge feature is observed that is derived from a transition from Sb $3d_{3/2}$ core levels to Sb 5s hybridized states in the conduction band. The primary absorption feature at the Sb M_{IV} edge arises from an Sb $3d_{3/2}$ → Sb 5p transition. The two features are not shifted in energy upon F-ion insertion consistent with the redox event primarily being centered on the iron centers. The change in intensity at the pre-edge results from a distortion of the local coordination geometry of Sb in going from a formally trigonal pyramidal SbO_3 to an expanded quasi-tetrahedral SbO_3F motif upon F-ion insertion.

To prove that fluoridation is not just a surface phenomenon, HAXPES measurements have been performed for the pristine, F-ion inserted, and defluoridated samples. The high incident photon energy of HAXPES increases the kinetic energy of the emitted electron and hence its mean free path, enabling interrogation of the bulk electronic structure.[19] **Figure 3A** provides unambiguous evidence for bulk oxidation of iron centers. A distinctive

feature characteristic of Fe centers with a +3 formal oxidation state emerges at a higher binding energy of 713 eV in high-resolution Fe $2p_{3/2}$ spectra upon F-ion insertion.[20] Treatment with *n*-BuLi reduces the iron centers back to the lower oxidation state of +2 with removal of F-ions attesting to the reversibility of the process at room temperature.

The Sb 3d high-resolution HAXPES spectra in **Figure 3B** shows a Sb $3d_{5/2}$ peak centered at *ca.* 530 eV for $FeSb_2O_4$, which corresponds to +3 oxidation formal state for Sb. No discernible oxidation is observed further corroborating that redox reaction is centered on the iron atoms. The F 1s HAXPES spectrum acquired for $FeSb_2O_4$ ($x \sim 1$) is further consistent with F-ions within the bulk of the material. The X-ray absorption and emission probes thus evidence bulk insertion and denote that the oxidative and reductive redox chemistry involved with F-ion insertion and de-insertion, respectively, occurs at the iron centers.

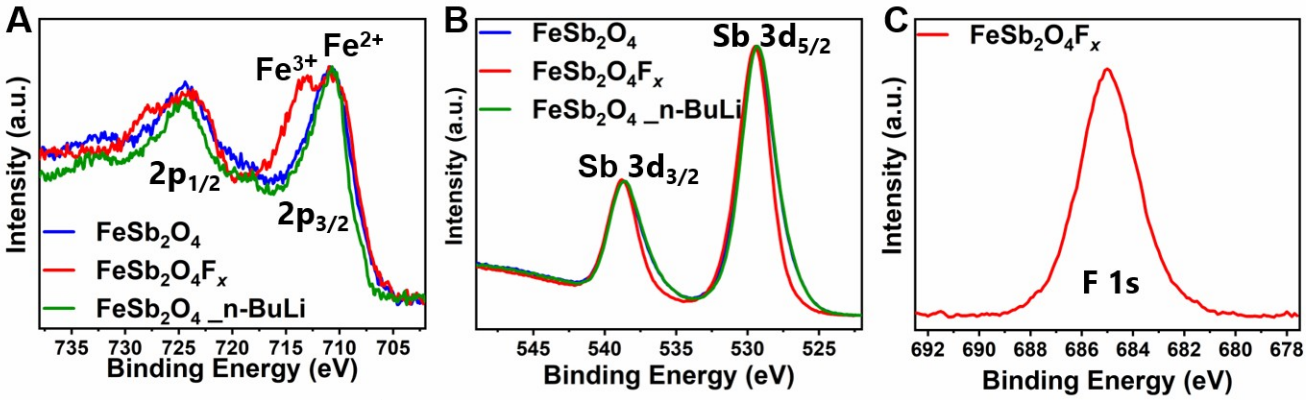

***Figure 3**. Electronic Structure Spectroscopy of $FeSb_2O_4$ before and After F-Ion Insertion. High-resolution HAXPES plots for A) Fe 2p, B) Sb 3d, and C) F 1s core excitations for $FeSb_2O_4$, $FeSb_2O_4F_x$ ($x \sim 1$), and $FeSb_2O_4$ recovered after treatment of $FeSb_2O_4F_x$ with n-BuLi.*

In addition to ensemble spectroscopy measurements, scanning transmission x-ray microscopy (STXM) has been performed at the Fe L-edge to evidence F-ion intercalation across individual particles analogous to the approach used to study lithiation gradients in Li_xFePO_4 and other battery

electrodes [11, 16, 19] **Figure 4A** and **B** present integrated STXM spectra and optical density images collected at the Fe L-edge for $FeSb_2O_4$ and $FeSb_2O_4F_x$ ($x \sim 1$) rods placed on X-ray transparent silicon nitride windows. The Fe L_{III}-edge spectrum for $FeSb_2O_4$ has a predominant feature at *ca.* 708 eV in **Figure 4A**, whereas, the main absorption feature for the $FeSb_2O_4F_x$ ($x \sim 1$) rods is observed at *ca.* 710 eV. These energy features are assigned to formal oxidation states of +2 and +3 in iron, respectively.[18] In other words, STXM imaging evidences oxidation of iron centers concomitant with F-ion insertion. The spatially resolved region-of-interest analysis in Figures 4C and D illustrate homogeneous oxidation of Fe centers across the particles, which resolves issues with inhomogeneous F-ion insertion, which have plagued other putative cathodes.

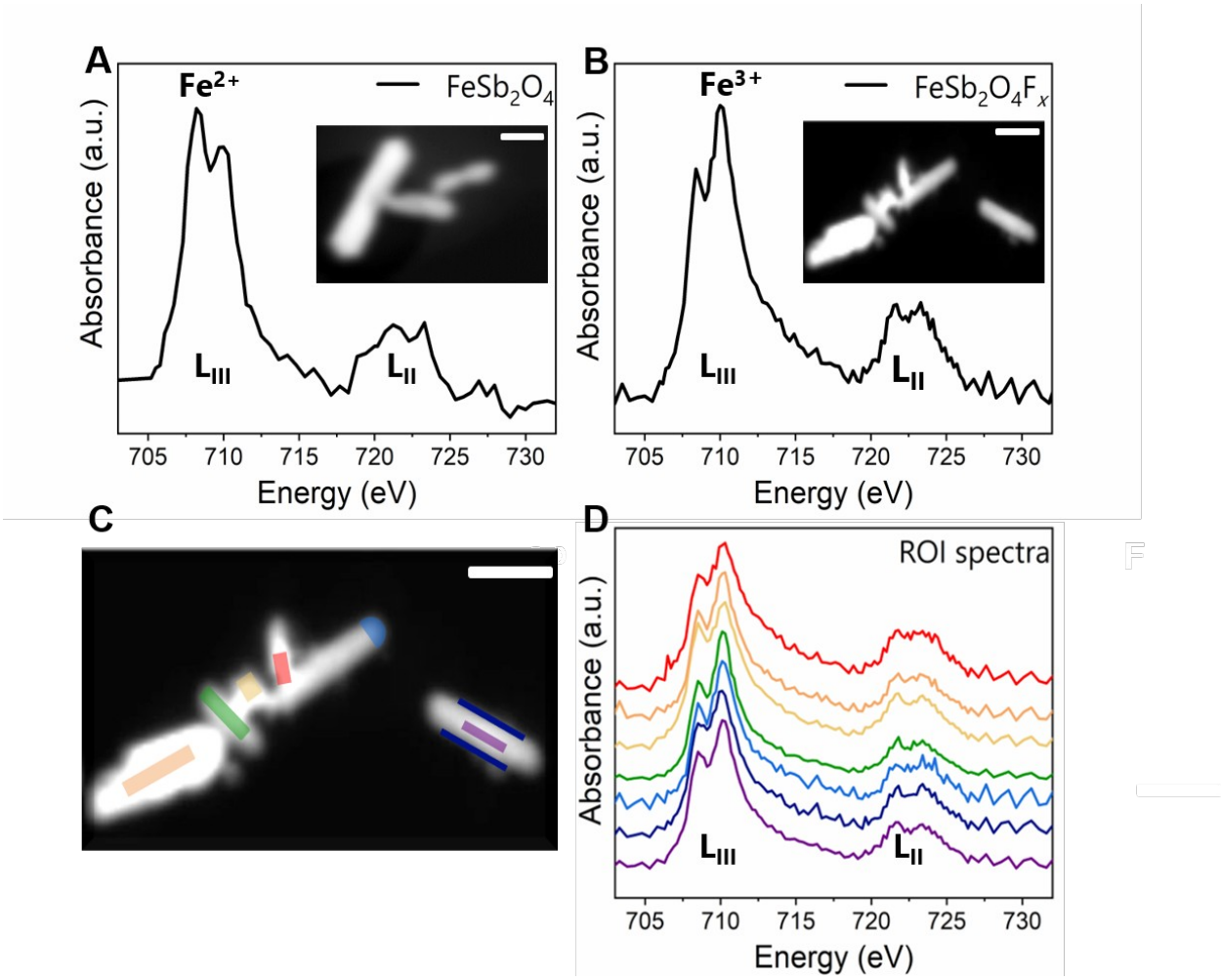

Figure 4. *Mapping Fe Oxidation State Across Individual $FeSb_2O_4F_x$ rods.* ***(A)*** *Fe $L_{3,2}$ edge STXM data obtained for $FeSb_2O_4$ rods. (Scale = 500 nm).* ***(B)*** *Fe $L_{3,2}$ edge STXM data obtained for $FeSb_2O_4F_x$ ($x \sim 1$) rods. (Scale = 1 μm).* ***(C)*** *Spatial regions of interest for the data shown in B.* ***(D)*** *Color-coded Fe L-edge spectra for regions highlighted in C.*

In conclusion, we have demonstrated the reversible insertion/de-insertion of F-ions from solution at room temperature in submicron-sized $FeSb_2O_4$ particles with full retention of crystallinity. The use of XeF_2 as a fluoridation source results in a high degree of fluoridation with $x \sim 1$ in $FeSb_2O_4$ corresponding to a F-ion for each redox-active Fe atom; F-ion insertion oxidizes iron centers from +2 to +3 and is observed to proceed homogeneously across the sub-micrometer-sized particles. Room temperature treatment with *n*-BuLi extracts the inserted F-ions, reduces trivalent iron back to divalent centers, and restores the pristine $FeSb_2O_4$ structure. The structural reversibility of $FeSb_2O_4$ upon F-intercalation/deintercalation and the <1% change in volume (which is in stark contrast to massive volume changes evidenced in conversion

batteries)[10] is a result of the availability of large 1D channels bound together by SbO_3 trigonal pyramids. F-ions are coordinated in the proximity of a pair of Fe and Sb sites inducing an anisotropic contraction of the tunnel. The use of XeF_2 and *n*-BuLi provides a robust scheme to achieve topochemical F-ion insertion and extraction for the screening of intercalation electrodes of next-generation anion battery materials. Future work will focus on achieving still higher concentrations of F-ion insertion and on mesostructuring of electrodes to resolve diffusion impediments.

ACKNOWLEDGEMENTS

This work was primarily supported by the National Science Foundation under DMR 1809866. The research was funded in part by award #A-1978-20190330 from the Welch Foundation. W.Z. and A.P. acknowledge support from the Advanced Light Source (ALS) doctoral fellowship in residence. The Advanced Light Source is supported by the Director, Office of Science, Office of Basic Energy Sciences, of the U.S. Department of Energy, under Contract No. DE-AC02-05CH11231. J.L.A. acknowledges support from a NASA Space Technology Research Fellowship under grant number 80NSSC17K0182. TAMU Materials Characterization Facility is acknowledged. Use of the TAMU Microscopy and Imaging Center is acknowledged.

REFERENCES

(1) Myung, S. T.; Maglia, F.; Park, K. J.; Yoon, C. S.; Lamp, P.; Kim, S. J.; Sun, Y. K. Nickel-Rich Layered Cathode Materials for Automotive Lithium-Ion Batteries: Achievements and Perspectives. *ACS Energy Lett.* **2017**, *2* (1), 196–223. https://doi.org/10.1021/acsenergylett.6b00594.

(2) Goodenough, J. B.; Park, K. S. The Li-Ion Rechargeable Battery: A Perspective. *J. Am. Chem. Soc.* **2013**, *135* (4), 1167–1176. https://doi.org/10.1021/ja3091438.

(3) Konarov, A.; Voronina, N.; Jo, J. H.; Bakenov, Z.; Sun, Y. K.; Myung, S. T. Present and Future Perspective on Electrode Materials for Rechargeable Zinc-Ion Batteries. *ACS Energy Lett.* **2018**, *3* (10), 2620–2640. https://doi.org/10.1021/acsenergylett.8b01552.

(4) Andrews, J. L.; Mukherjee, A.; Yoo, H. D.; Parija, A.; Marley, P. M.; Fakra, S.; Prendergast, D.; Cabana, J.; Klie, R. F.; Banerjee, S. Reversible Mg-Ion Insertion in a Metastable One-Dimensional Polymorph of V2O5. *Chem* **2018**, *4* (3), 564–585. https://doi.org/10.1016/j.chempr.2017.12.018.

(5) Yadav, G. G.; Turney, D.; Huang, J.; Wei, X.; Banerjee, S. Breaking the 2

v Barrier in Aqueous Zinc Chemistry: Creating 2.45 and 2.8 v MnO2-Zn Aqueous Batteries. *ACS Energy Lett.* **2019**, *4* (9), 2144–2146. https://doi.org/10.1021/acsenergylett.9b01643.

(6) Wang, N.; Chu, C.; Xu, X.; Du, Y.; Yang, J.; Bai, Z.; Dou, S. Comprehensive New Insights and Perspectives into Ti-Based Anodes for Next-Generation Alkaline Metal (Na+, K+) Ion Batteries. *Adv. Energy Mater.* **2018**, *8* (27), 1–27. https://doi.org/10.1002/aenm.201801888.

(7) Gu, S.; Wang, H.; Wu, C.; Bai, Y.; Li, H.; Wu, F. Confirming Reversible Al3+ Storage Mechanism through Intercalation of Al3+ into V2O5 Nanowires in a Rechargeable Aluminum Battery. *Energy Storage Mater.* **2017**, *6*, 9–17. https://doi.org/10.1016/j.ensm.2016.09.001.

(8) Anji Reddy, M.; Fichtner, M. Batteries Based on Fluoride Shuttle. *J. Mater. Chem.* **2011**, *21* (43), 17059–17062. https://doi.org/10.1039/c1jm13535j.

(9) Gschwind, F.; Rodriguez-Garcia, G.; Sandbeck, D. J. S.; Gross, A.; Weil, M.; Fichtner, M.; Hörmann, N. Fluoride Ion Batteries: Theoretical Performance, Safety, Toxicity, and a Combinatorial Screening of New Electrodes. *J. Fluor. Chem.* **2016**, *182*, 76–90. https://doi.org/10.1016/j.jfluchem.2015.12.002.

(10) Thieu, D. T.; Fawey, M. H.; Bhatia, H.; Diemant, T.; Chakravadhanula, V. S. K.; Behm, R. J.; Kübel, C.; Fichtner, M. CuF2 as Reversible Cathode for Fluoride Ion Batteries. *Adv. Funct. Mater.* **2017**, *27* (31), 1–11. https://doi.org/10.1002/adfm.201701051.

(11) De Laune, B. P.; Rees, G. J.; Marco, J. F.; Hah, H. Y.; Johnson, C. E.; Johnson, J. A.; Berry, F. J.; Hanna, J. V.; Greaves, C. Topotactic Fluorine Insertion into the Channels of FeSb2O4-Related Materials. *Inorg. Chem.* **2017**, *56* (16), 10078–10089. https://doi.org/10.1021/acs.inorgchem.7b01613.

(12) Nowroozi, M. A.; Wissel, K.; Rohrer, J.; Munnangi, A. R.; Clemens, O. LaSrMnO4: Reversible Electrochemical Intercalation of Fluoride Ions in the Context of Fluoride Ion Batteries. *Chem. Mater.* **2017**, *29* (8), 3441–3453. https://doi.org/10.1021/acs.chemmater.6b05075.

(13) De Jesus, L. R.; Andrews, J. L.; Parija, A.; Banerjee, S. Defining Diffusion Pathways in Intercalation Cathode Materials: Some Lessons from V2O5 on Directing Cation Traffic. *ACS Energy Lett.* **2018**, *3* (4), 915–931. https://doi.org/10.1021/acsenergylett.8b00156.

(14) Gonzalo, J. A.; Cox, D. E.; Shirane, G. The Magnetic Structure of FeSb2O4. *Phys. Rev.* **1966**, *147* (2), 415–418. https://doi.org/10.1103/PhysRev.147.415.

(15) Ramsden, C. A. Xenon Difluoride in the Organic Laboratory: A Tale of

Substrates, Solvents and Vessels. *Arkivoc* **2013**, *2014* (1), 109–126. https://doi.org/10.3998/ark.5550190.p008.436.

(16) Wang, J.; Yang, J.; Tang, Y.; Li, R.; Liang, G.; Sham, T. K.; Sun, X. Surface Aging at Olivine LiFePO4: A Direct Visual Observation of Iron Dissolution and the Protection Role of Nano-Carbon Coating. *J. Mater. Chem. A* **2013**, *1* (5), 1579–1586. https://doi.org/10.1039/c2ta00521b.

(17) Murugesan, V.; Cho, J. S.; Govind, N.; Andersen, A.; Olszta, M. J.; Han, K. S.; Li, G.; Lee, H.; Reed, D. M.; Sprenkle, V. L.; et al. Lithium Insertion Mechanism in Iron Fluoride Nanoparticles Prepared by Catalytic Decomposition of Fluoropolymer. *ACS Appl. Energy Mater.* **2019**, *2* (3), 1832–1843. https://doi.org/10.1021/acsaem.8b01983.

(18) Ohmer, N.; Fenk, B.; Samuelis, D.; Chen, C. C.; Maier, J.; Weigand, M.; Goering, E.; Schütz, G. Phase Evolution in Single-Crystalline LiFePO4 Followed by in Situ Scanning X-Ray Microscopy of a Micrometre-Sized Battery. *Nat. Commun.* **2015**, *6*, 1–7. https://doi.org/10.1038/ncomms7045.

(19) Weiland, C.; Rumaiz, A. K.; Pianetta, P.; Woicik, J. C. Recent Applications of Hard X-Ray Photoelectron Spectroscopy. *J. Vac. Sci. Technol. A Vacuum, Surfaces, Film.* **2016**, *34* (3), 030801. https://doi.org/10.1116/1.4946046.

(20) Grosvenor, A. P.; Kobe, B. A.; Biesinger, M. C.; McIntyre, N. S. Investigation of Multiplet Splitting of Fe 2p XPS Spectra and Bonding in Iron Compounds. *Surf. Interface Anal.* **2004**, *36* (12), 1564–1574. https://doi.org/10.1002/sia.1984.

(21) De Jesus, L. R.; Stein, P.; Andrews, J. L.; Luo, Y.; Xu, B. X.; Banerjee, S. Striping Modulations and Strain Gradients within Individual Particles of a Cathode Material upon Lithiation. *Mater. Horizons* **2018**, *5* (3), 486–498. https://doi.org/10.1039/c8mh00037a.